

ORIGINAL ARTICLE

ABH damping of monolithic silica glass cantilever by structural and material modification using fs laser micromachining

Kana Tomita¹  | Tetsuo Kishi¹  | Tetsuji Yano¹ | Pieter Vlugter² | Yves Bellouard² 

¹Department of Materials Science and Engineering, Tokyo Institute of Technology, Tokyo, Japan

²Galatea Laboratory, IMT/STI, Ecole Polytechnique Fédérale de Lausanne (EPFL), Neuchâtel, Switzerland

Correspondence

Tetsuo Kishi, Department of Materials Science and Engineering, Tokyo Institute of Technology, Meguro-ku, Tokyo, Japan.
Email: tkishi@ceram.titech.ac.jp

Abstract

Combining femtosecond laser exposure with chemical etching enables the fabrication of arbitrary 3D shapes in fused silica with micron precision. Here, we investigate the use of this process combined with additional tuning of the material properties for controlling the vibrational behavior of silica microcantilevers through an acoustic black hole (ABH) effect. This effect, caused by a tapered profile at the cantilever's end, enables the trapping of propagating acoustic waves. Such cantilevers with ABH design show a remarkable amplitude decrease in the resonance peak without adding any damping material as demonstrated experimentally. Finally, using Fourier-transform infrared spectroscopy (FTIR), we observe residual effects of the laser exposure at the surface of the specimen that have noticeable influence on the dynamic behavior of the device.

KEYWORDS

femtosecond laser processing, IR spectroscopy, leaching, silica glass, surface modification

1 | INTRODUCTION

Fused silica has outstanding physical characteristics, such as high transparency, low intrinsic loss, and outstanding elastic properties, for micromechanical devices. Thanks to the microfabrication technique based on femtosecond laser-induced selective etching,¹ highly complex 3D microstructures can be carved out of single glass substrate.^{2–4} This manufacturing process brings great opportunities in the field of microdevices such as MEMS, microfluidics system, and so on. One of the advantages of this fabrication process is its ability to combine, not only structural elements of various kinds but also optical ones in a single monolith. This process circumvents separating the bonded layers by mechanical damages such as repetitive vibration. Control of static and dynamic behavior of the entire MEMS structure takes an important role.⁵

Mechanical vibrations at the resonance may compromise the stability of a device, when it is undesired and uncontrolled as a result of extrinsic noise excitations. To broaden their usable frequency ranges, notably by reducing the vibration amplitude for a given set of frequencies, the concept of ‘acoustic black hole’ (ABH) was proposed.^{6,7} There, it was shown that a plate with an acute angle wedge has less frequency dependence on vibrations.^{6,8} In particular, it was theoretically proven that a wedge with a profile defined by a power law shows effective damping. V. V. Krylov demonstrated this effect experimentally with a ‘meter-sized’ steel plate.⁹ This approach is particularly attractive in aeronautics and for automotive applications,¹⁰ as in both cases, excitations of resonant modes can have dramatic effects if undamped. Likewise, applying this method at the microscale will enable noise attenuation from resonant vibrations in various types

of microsystems without the need for additional processing steps to add damping material.

Scaling ABH phenomenon down to the microscale is not just a matter of size, since slight inhomogeneity or defects of material as well as fabrication imperfections, most often negligible at meter-scale may have dramatic consequences at the microscale. Therefore, implementing ABH at the microscale requires a detailed analysis of the material properties after the fabrication process as well as high fabrication dimensional resolution and accuracy. While 3D microfabrication of fused silica using femtosecond laser may realize enough preciseness according to numerous optimization reports for irradiation conditions,^{11–14} the effects of the laser at the atomic level are not fully understood as it is difficult to see the detailed gradation of material properties after writing complex patterns inside the material.¹⁵ In addition, the effects on material properties, such as thermal expansion coefficient,¹⁶ Young's modulus,^{17,18} and density,^{19,20} after the etching process are not revealed. Further understandings on these mechanisms will enhance its reliability and broaden application fields.

In this study, a silica glass cantilever implementing an ABH effect was fabricated by a combination of nonablative femtosecond laser exposure and chemical etching. The vibration behavior of cantilever was observed and analyzed by comparing the experimental observations with theoretical calculations. In order to investigate the cause of disagreement between experiments and theory, surface-properties change, including texture, roughness, and chemical bonding state, was considered. While we found a reasonable agreement between theory and experiments in the overall behavior of the device, we also noticed significant differences that highlight the importance of subtle surface properties changes resulting from the fabrication process on the cantilever dynamic behavior.

1.1 | Theory of acoustic black hole effect and cantilever design

The followings are a brief review of the theoretical aspects behind the ABH phenomenon. Flexural waves in a beam are governed by the following equation:

$$\frac{\partial^2}{\partial x^2} \left(D(x) \frac{\partial^2 W}{\partial x^2} \right) - \omega^2 \rho h(x) W = 0 \quad (1)$$

where W stands for the displacement along the z -axis (see Figure 1), ρ for the density of the material of the vibrating beam, ω for the angular frequency, and finally, $D(x)$ for the bending stiffness. The bending stiffness of the beam with a rectangular cross-section is further expressed as:

$$D(x) = \frac{Eh(x)}{12(1-\nu^2)} \quad (2)$$

$$h(x) = \begin{cases} (h_c - h_{Tip}) \left(\frac{x}{L_{Taper}} \right)^m + h_{Tip}, & 0 < x < L_{Taper} \\ h_c, & L_{Taper} < x < L_c \end{cases} \quad (3)$$

where E is Young's modulus, $h(x)$ is the thickness of cantilever at a position x along the beam, ν is the Poisson's ratio, and m is an exponent that defines the slenderness of the edge. In this experiment, cantilever with the tapering edge, which ABH effect can theoretically be obtained, was designed and fabricated. A solution of Equation 1 can be expressed as follows:

$$W(x) = A(x) e^{i\Phi(x)} \quad (4)$$

where $A(x)$ is the displacement in each point of the beam and $\Phi(x)$ is the phase difference between the excitation wave and the propagating wave in the beam. In the case of a cantilever in vacuum, the local wavenumber k is further defined by:

In practice, it is difficult to achieve a zero thickness at the

$$k(x, \omega) = \left(\frac{12\rho(1-\nu^2)}{E} \right)^{\frac{1}{4}} \left(\frac{1}{\omega h(x)} \right)^{1/2} \quad (5)$$

tip. To a certain extent, the beam edge is always truncated with a minimum tip thickness h_{Tip} . The phase increment $\phi(x)$ between 0 and x , writes:

$$\phi(x) = \int_0^x k(x) dx \quad (6)$$

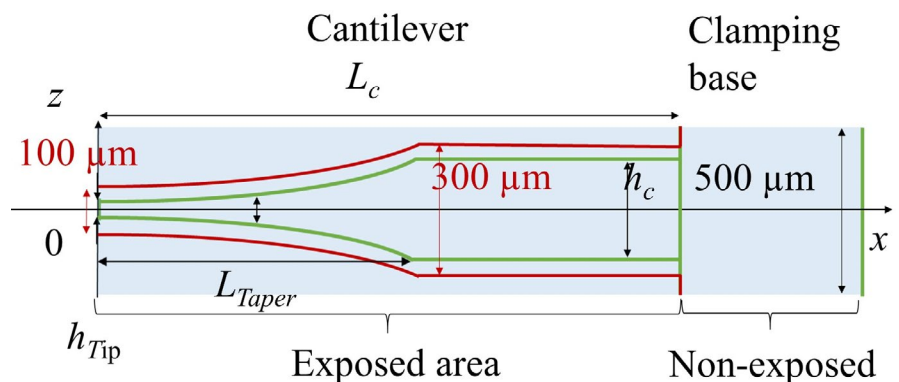


FIGURE 1 Dimension of cantilever and position inside silica glass substrate. Laser-irradiated surface in red line and actual surface in green line [Color figure can be viewed at wileyonlinelibrary.com]

For a coefficient $m \geq 2$ (see Equation 3), the phase difference increment diverges as x increases. This means that a flexural wave propagating in the beam never reaches the edge.⁸ As the energy is dissipated through dynamic deformation, a phase difference between stress and strain is observed. In such a case, the Young's modulus is expressed in a complex form: $E^* = E_0 (1 - i\eta_0)$. Consequently, the reflection coefficient R will decrease and result in an ABH effect.

$$R = \exp\left(-2 \int_0^x \text{Im}k(x) dx\right) \quad (7)$$

where $\text{Im}k = \frac{1}{4\eta_0} \text{Re}k$ and η_0 is the intrinsic loss factor of the material.

The ABH theory assumes that the wave fully propagates toward the edge, without partial reflection. This assumption is valid for a slowly varying thickness profile at the tip of the cantilever. In practice, fabricating such slender profiles is difficult to achieve at the microscale with conventional manufacturing processes, such as lithographic ones, as this design is intrinsically three dimensional. To overcome this challenge, we took advantage of the femtosecond laser micro-machining of glass substrates. The design of the silica glass cantilever is shown in Figure 1.

Based on Equations 3, 5, and 7, the increase in m seems to be the most efficient way to have a greater attenuation effect. A larger m in the profile function generates an abrupt change in the thickness at the start point of ABH design. In our design, $m = 2$ is chosen and we assume that the obtained geometrical profile has enough smoothness to avoid counter-propagating waves at the boundary between the tapered and the flat part. In such conditions, the design is fulfilling the normalized wavenumber variation given in Ref. [21]:

$$\frac{dk}{dx} \frac{1}{k^2} \ll 1 \quad (8)$$

This criterion indicates that the change in wavenumber must be smaller over distances comparable to the wavelength. In this way, the incident wave fully propagates toward the tip of the cantilever without loss at the beginning of the tapered section of the profile.

2 | EXPERIMENTAL PROCEDURES

2.1 | Cantilever fabrication

The principle is to sequentially use a nonablative femtosecond exposure process and a chemical etching step.^{22,23} The cantilever was fabricated out of a 500- μm -thick silica

substrate (Corning 7980-0F). The substrate contains 1000-ppm OH and traces of Cl in the order of 100 ppm (Class-III fused silica). For femtosecond laser irradiation, we used a Yb-fiber amplifier ($\lambda = 1030$ nm) emitting at a rate of 800 kHz, 230 nJ pulses of duration 270 fs. Scanning velocity was 10 mm/s (corresponding to 80 pulses deposited in 1 μm distance along the writing direction). The polarization was always set perpendicular to the writing direction. To focus the laser beam, we used an objective with a numerical aperture of 0.4. The focal spot volume has an approximated ellipsoidal shape with a short axis width of 1.6, and 10 μm for the long axis, oriented towards the beam optical propagation axis (ie, the z -axis direction).²² The contour of the cantilever was defined with a set of adjacent straight lines, as shown in Figure 2. Spacing between lines was 1 μm in the x -axis direction and 10 μm along the z -axis direction. Those distances were optimized for efficient etching.¹² After exposure, the specimen is immersed in a low-concentration HF bath (2.5%) until all the previously exposed volume dissolved, and the surrounding bulk falls off. Soak time was about 10 hours for cantilever without tapered profile and 40 hours for the one with a tapered end.

2.2 | Vibration tests

The cantilever shows a resonant vibration with simple dynamic deformation. The resonant frequency can be expressed as function of material constants. In the case of a planar cantilever without tapered end, the resonant frequency f_n writes:

$$f_n = \frac{1}{2\pi} \beta_n^2 \frac{h}{L^2} \sqrt{\frac{E}{12\rho}} \quad (9)$$

where n is the vibration order for a given mode n , β_n is a constant depending on the mode, h and L are thickness and length

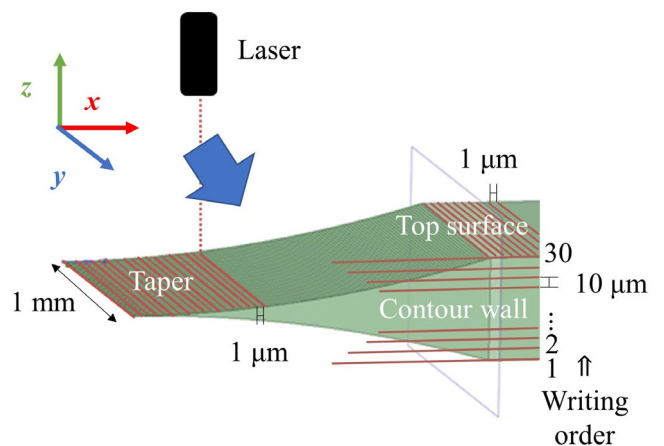


FIGURE 2 Schematic illustration of laser scanning process to pick out the tapered cantilever of the silica glass substrate [Color figure can be viewed at wileyonlinelibrary.com]

of the cantilever, respectively, E is the Young's modulus, and ρ is the density of the cantilever material. In the case of the cantilever with a taper design, the resonant frequency cannot simply be obtained from the analytical formula of Equation 9, but rather through simulation.

Here, we focused on the first mode of vibration for each cantilevers. A triangulation laser sensor (Keyence LK-H022K) was used to measure the cantilever tip deflections at a sampling frequency of 50 kHz. The cantilevers were set on a plate itself mounted on a piezoelectric actuator (Noliac, NAC2003). An AC voltage of 100 mVpp was applied to the actuator, and its frequency was swept from 2000 to 3700 Hz for $n = 1$ (primary mode) in Equation 9. The dynamic behavior of the cantilever with a tapered end at the resonant frequency was simulated by the Finite Element Method using COMSOL® using the measured dimensional parameters of the actual, fabricated cantilevers, and compared with the experimental values. In our simulations and calculations, the relevant material constants were $E = 72.5$ GPa, $\rho = 2201$ kg/m³, and $\nu = 0.17$.

Ring down measurements consisting of exciting the cantilever to its resonant frequency and subsequently turning off the vibration source, followed by monitoring vibration amplitude decay, were performed to further evaluate the vibration damping behaviors. The measurement of the decay time provides an estimate of the ABH-induced attenuation. The amplitude decay curves showed a single exponential decay in early stage.

2.3 | Static properties observation of the cantilever after processing

Surface profile $h(x)$ of the fabricated cantilever was measured by a stylus profiler (Dektak) to evaluate the precision of the micromachining. The stylus radius was set to 12.5 μm and scan speed was 0.133 $\mu\text{m/s}$. The center of the cantilever was scanned along the x -axis. The front and backside were measured separately. The measured profile of the tapered part was fit by a function of $h(x) = ax^m + b$, where a is a proportional constant of the power function and m is the exponent of fit function. As a preprogrammed design, $m = 2$ for all designs.

The surface roughness of the cantilever surface was observed and measured by a laser microscope (VK-8510, Keyence Corporation). Roughness was evaluated using the Arithmetical mean deviation R_a value of the horizontal and vertical direction of the cantilever.

Fourier transform infrared (FTIR) reflection spectra for the sample surface were measured at room temperature in the wavenumber range 600–4500 cm^{-1} by a micro-FTIR spectrometer (JASCO, FT/IR-6100, IRT-5000). The aperture size

was 50 $\mu\text{m} \times 50 \mu\text{m}$ and resolution was 4 cm^{-1} . Spectra were obtained from 3 different cantilevers.

3 | RESULTS

3.1 | Geometrical profile of cantilever after processing

The thickness of tip at the end of cantilever h_{Tip} and flat part h_c was measured by observing the cross section in an optical microscope. The thickness profile of the tapered cantilever was fit with the Least-square method to compare the profile function of the exposed pattern with the end-product, ie, the fabricated cantilever. Results are shown in Table 1. Tapered part thickness was designed to decrease quadratic function ($m = 2$). All cantilevers had almost the same thickness at the tip and flat part, and m value after fitting was found in the range 1.86–2.01. The change in thickness at the base (Nonexposed) before and after etching was less than 10 μm . The profile result shows a good agreement of the surface profile between the design and the fabricated cantilever. The typical thickness h_{Tip} and h_c were always about 25 μm smaller than the laser-irradiated line for all samples, regardless of the etching time.

To check the quality of the surface smoothness, the roughness of the cantilever surface was observed. The bottom of Figure 3 shows the optical microscope images of the sample surface. In the laser exposed area, the periodic texture is similar to a texture reported in Ref. [4]. In contrast, the nonexposed area showed a clear flat surface. Table 2 shows the R_a of the flat part of the cantilever (laser exposed), and the base part of the sample (unexposed), respectively. These values were in good agreement with microscopic image in Figure 3, showing that the exposed surface has rough surface due to laser exposure even after etching.

3.2 | Vibration measurement

The resonant frequency was measured and compared with the simulation results. The results are shown in Figure 4.

TABLE 1 Measured dimensions of the fabricated cantilevers with different L_{Taper}

$L_{\text{Taper}}/\text{mm}$	$h_{\text{Tip}}/\mu\text{m}$	$h_c/\mu\text{m}$	m
0	-	250	-
3.33	54.2 ± 1.0	251 ± 1	1.86
5.00	53.9 ± 0.8	250 ± 3	2.00
5.65	56.1 ± 0.4	249 ± 2	1.99
8.57	58.8 ± 0.8	252 ± 1	2.01

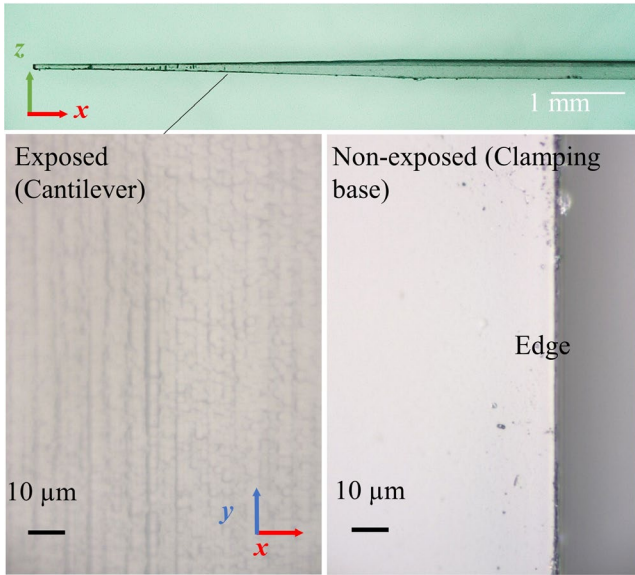


FIGURE 3 Appearance of the fabricated cantilever with tapering. Top: side view of fabricated cantilever ($L_{Taper} = 5$ mm). Bottom: microscopic photographs of laser-exposed surface (left) and nonexposed one (right) of cantilever [Color figure can be viewed at wileyonlinelibrary.com]

TABLE 2 Typical values of the surface roughness R_a (in μm) measured on the cantilever

	Non-exposed	Exposed
Along x-axis (50 μm)	0.02	0.097
Along y-axis (50 μm)		0.107

The calculated values are the frequencies of the primary vibration mode ($n = 1$ in Equation 9), which corresponds to a deflection aligned along the z -axis, with a static-node at the fixed end. The dependence of L_{Taper} on the resonant frequency showed the same trends in both experimentally measured and simulated values. The simulations with three different models were done in order to find out the most effective parameters affecting the values of the resonant frequency.

The first model, shown with a smooth line in Figure 4, had average dimensions among fabricated cantilever as follow: $h_{Tip} = 55 \mu\text{m}$, $h_c = 250 \mu\text{m}$, and $m = 2$ (Model A1). To account for the error due to the profile function change during the fabrication process, $m = 1.8$ with the same dimension (Model A2) was also simulated. The resonant frequency difference between these 2 models was within 4%, which is smaller compared to the difference between the simulated frequencies of two models (Model A1 and A2) and their experimental values. The experimental frequency was 3%-10% lower compared to simulation. Model B with the dimensions shown in Table 1 was plotted with asterisk mark for $L_{Taper} = 3.3, 5.0, 5.7, 8.6$. Although the fabricated Model B

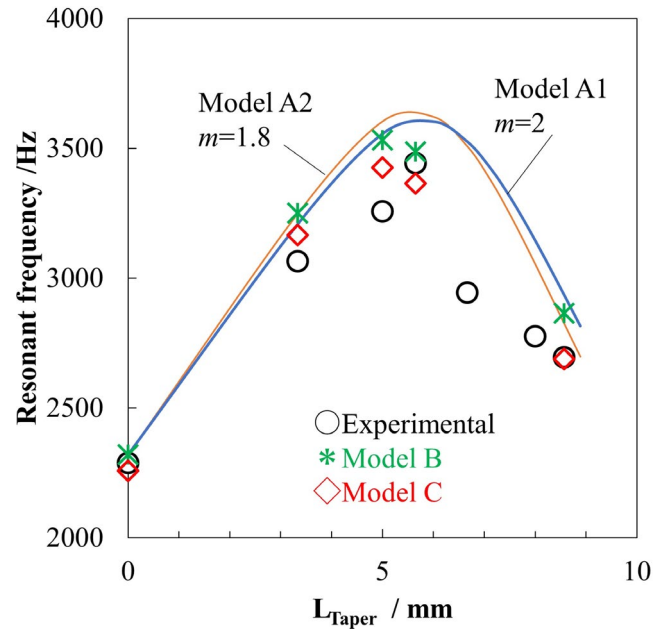


FIGURE 4 Experimental and simulated resonant frequency of each cantilever with various taper length. Model A1 and A2 show simulation results using average cantilever dimensions with different function parameter m . Model B is simulated with the measured dimensions for each cantilever with uniform Young's modulus. Model C shows the simulation results on the cantilever with lower Young's modulus surface layers of $E_{surface} = 60$ GPa of $10 \mu\text{m}$ thickness [Color figure can be viewed at wileyonlinelibrary.com]

had more accurate dimensions compared to the desired profile, the resonant frequency was still estimated higher compared to its experimental value.

Figure 5 shows the results of the vibration test for a tapered ($L_{Taper} = 5.0$ mm) and a nontapered cantilever, respectively. (A) is the Fourier transformed spectrum of the amplitude obtained by the frequency sweep test. The frequency is normalized with the resonant frequency f_0 . The tapered cantilever shows a broader resonant peak; The FWHM of each resonant peak was 1.5 Hz ($\Delta f/f_0 = 4.6 \times 10^{-4}$) for tapered cantilever and 0.8 Hz ($\Delta f/f_0 = 3.5 \times 10^{-4}$) for cantilever without taper. This means the cantilever amplitude had a lower resonant frequency dependence.

Figure 5B shows the typical result of ring down measurement. The deflection amplitude decay after the resonant vibration of the nontapered cantilever and the tapered cantilever ($L_{Taper} = 5$ mm), respectively. The cantilever with an ABH effect attenuated over a shorter period compared to the nontapered one. The tapered cantilever showed a damping effect without any additive absorbing material demonstrating the concept of ABH. A fitting function $A \cdot e^{-\pi \frac{t}{Q}}$ was applied on the decay curves to extract the Q factor, which indicates the acuity of a resonant vibration peak. The Q factors obtained for each cantilever with different L_{Taper} (0-8.6 mm) are plotted in Figure 6. The Q factor decreases as the tapered length gets longer, which shows an increase

FIGURE 5 (A) Frequency spectra obtained by Fourier transformation of vibration amplitude-wave form in Sweep test. (B) Decay curves of vibration amplitude after resonant vibration in Ring down measurement [Color figure can be viewed at wileyonlinelibrary.com]

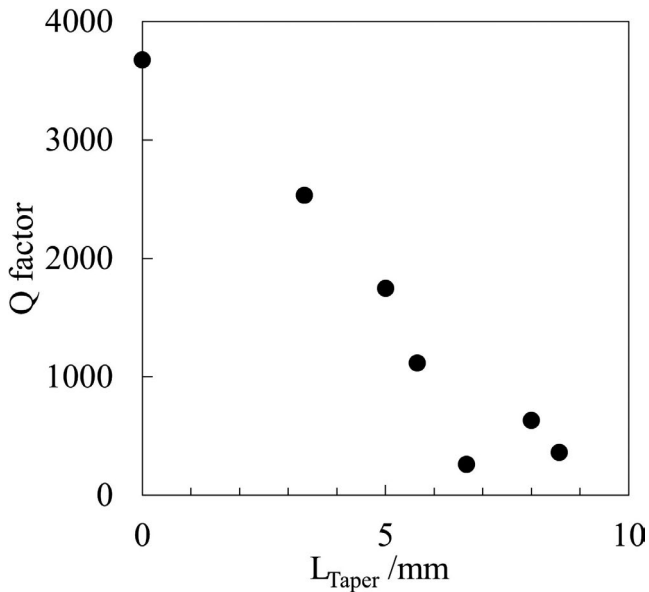
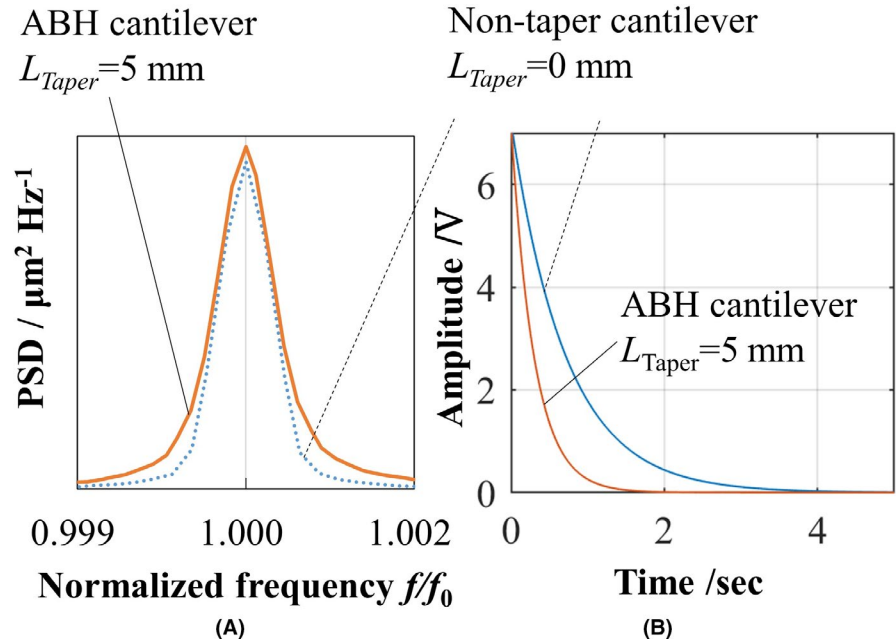


FIGURE 6 Experimental Q factor obtained by fitting decay curve from Ring down measurement into the function $A \cdot e^{-\pi \frac{t}{Q}}$

in attenuation efficiency with a larger proportion of ABH design.

3.3 | Chemical properties of the surface after processing

The FTIR reflectance spectrum of the one cantilever surface of three different samples is shown in Figure 7. The spectra from the three different cantilevers showed the same trends.

The absorption spectra were obtained using the Kramers-Kronig transformation applied to the corresponding

reflectance spectra. A significant peak around 1110 cm^{-1} shows the asymmetric stretch band of Si-O-Si bonding.²⁴ The average position of peak around 1100 cm^{-1} showed distinctive dependence on surface condition. Original silica substrate before etching had the peak at $1109.5 \pm 0.3 \text{ cm}^{-1}$. After etching, $1108.9 \pm 0.5 \text{ cm}^{-1}$ for nonexposed and 1111.4 ± 0.7 for exposed surface. Although average peak position was almost constant for nonexposed surface before and after etching, peak position of exposed surface shifted to higher wavenumber side.

The peak around 3600 cm^{-1} is related to the presence of OH groups. This peak gets emphasized on the exposed surface. Peak around area I (2000 cm^{-1}) and area II (2233 cm^{-1}) were also detected only on exposed surface, which is assigned to Si-H bond.^{25,26}

4 | DISCUSSION

Silica glass cantilever with various taper length showed vibrational attenuations in the frequency range around 2.5–3.5 kHz. The ABH design was successfully implemented by taking advantage of the precise control of the thickness profile at the microscale using femtosecond laser and wet-etching microprocessing. To date, the experimental investigations of ABH had been limited for meter-scale structure in metal or in composite materials. The result shown in this report broadens the capability of the ABH effect.

To handle the vibrational behavior of microstructures, it is necessary to control both the preciseness of the structural profile and the materials properties. Therefore, a particular attention was paid on the effects of the fabrication process on fused silica for further understanding possible factors

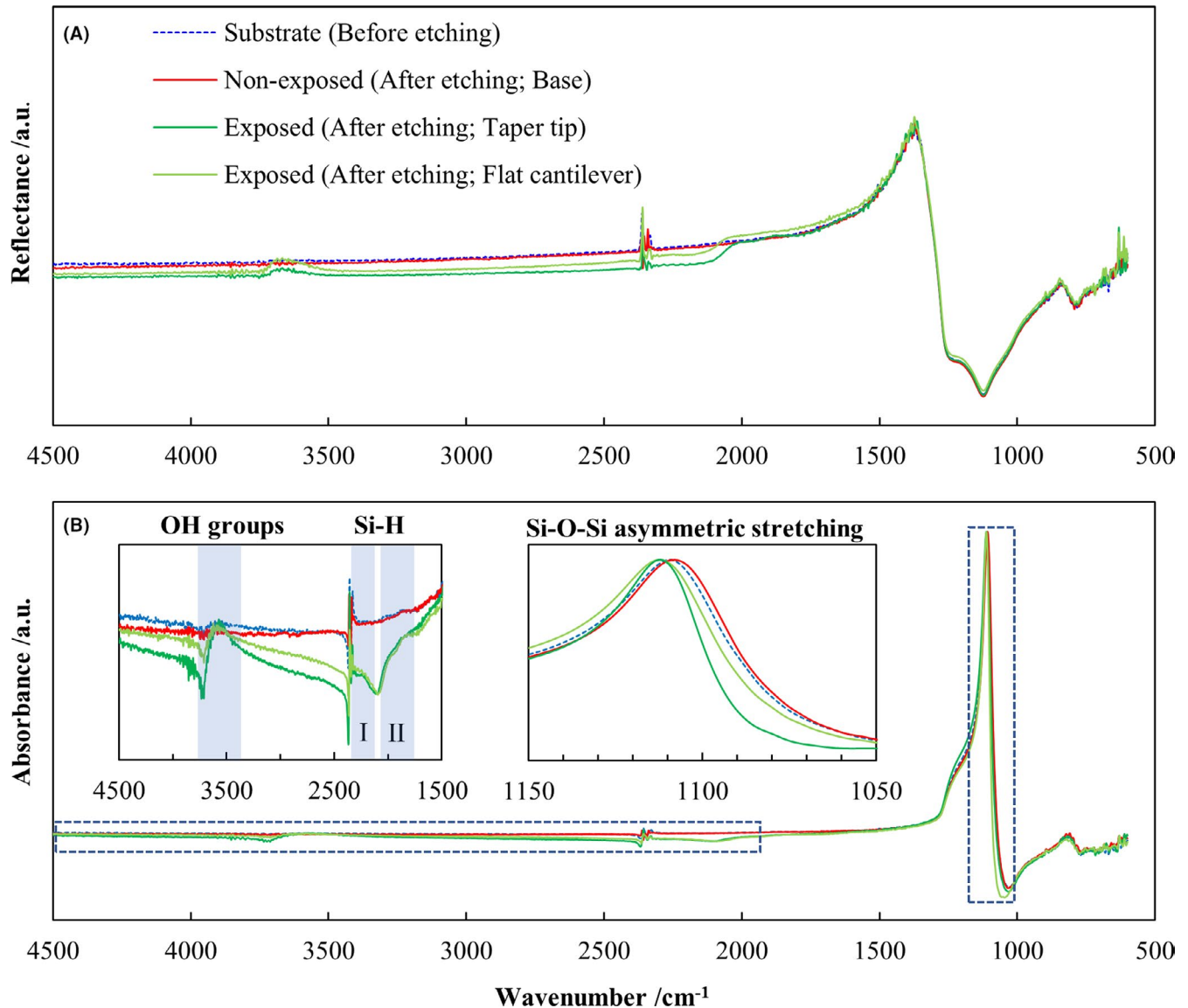


FIGURE 7 Micro-IR spectra before and after etching. (A) Specular reflection spectra and (B) Absorption spectra obtained by Kramers-Kronig transformation. Green and red solid lines are the laser-exposed and nonexposed surface after etching, respectively. Blue broken line indicates the initial sample before treatment. Insets represent the expanded spectra of the respective vibration regions [Color figure can be viewed at wileyonlinelibrary.com]

affecting vibrational behaviors. Here, we analyze the vibration characteristics, such as resonant frequency and energy dissipation factors, by comparing experimental and calculated results.

4.1 | Fabrication profile evaluation by ABH implementation

The actual surface of cantilever after etching was always below the programmed design, although the reduction rate was nearly constant among all samples. Typical dimension values, such as tip thickness h_{Tip} , were 53.9–58.8 μm , cantilever thickness at flat part h_c was 249–252 μm , as shown in

Table 1. There were always about 40–50 μm in total thickness reduction compared to the original design. The function of thickness profile was kept as a quadratic function within 93%–100% accuracy based on m value obtained from surface profile scanning.

Vibrational behavior supports the accuracy of the 3D cantilever outline. The ABH effect was observed for the cantilever with the tapered thickness profile since this effect is only attainable with a smooth and accurate profile, as shown in Equation 6.

Even though with an accurate outline profile of the fabricated cantilever, the measured resonant frequency could not be obtained from simulation. As shown in Figure 4 with several models, a frequency difference degree of 100 Hz that

cannot be related to the deviations from the designed profile was observed. Therefore, material properties used in the simulation, such as Young's modulus, Poisson's ratio, and density, can be the reasonable factor that may cause such difference.

4.2 | Material properties change resulting from manufacturing

As shown in Figure 4, the experimental values for the resonant frequency were always lower compared to the simulated ones. As shown in the result comparing both, the gap between design and actual profile would not make such a significant difference. Here, we consider the origin of this disagreement as a residual material property change due to laser exposure, as the change was observed only at the exposed surface after processing.

First of all, the femtosecond laser irradiation condition in the fabrication process leads to the formation of nanogratings that consists of self-organized texture parallel to one another as can be observed in SEM images.^{22,27} A significant change in refractive index (consisting on a periodic modulation of its value in the laser-affected zone) is generated in highly localized ellipsoidal volume that are 10- μm high along the laser-induced direction and about 2 μm wide along the waist.¹ The critical mechanism of high aspect ratio etching of fused silica is not fully understood.^{13,15,28} Intense irradiation of femtosecond laser induces defects in silica such as NBOHC and ODC (II)²⁹ that show broad fluorescence in the visible wavelength region. However, no fluorescence was found after the etching process by Raman spectrum measurement using an excitation laser with a wavelength of 532 nm. This observation suggests that the exposed volume containing these defects have been dissolved or chemically changed. The material property profile in higher resolution compared to laser focal point is not yet measured. Residual effect after etching is not yet figured out in detail.

In the case of the same microfabrication process reported in a previous study,¹² the laser drawing spacing in z -axis direction is less than 18 μm results in a higher etching rate of over 90 $\mu\text{m}/\text{hour}$. The etching rate decreases by 99% when the spacing is more than 21 μm . Similarly, in this report, etching always stopped at 20–25 μm below the laser irradiation line (about 50 μm reduction in thickness, 20–25 μm , respectively, for top and bottom side), and this reduction was independent of etching time. These results indicate that laser affected modification around 20 μm away from the focal point has essential effect on etching mechanism.

We now turn our attention to the results obtained in this study. The surface condition was different among laser exposed and nonexposed surface after processing. From the FTIR measurement shown in Figure 7, spectrum differences between

exposed and nonexposed surface after etching can be clearly observed. Reflectance spectra of exposed surface showed noticeable shoulder at 2000 cm^{-1} as shown in Figure 7A. The same trend was found on both taper and flat part of 3 different cantilevers' surface, but never found on nonexposed surface.

As shown in absorbance spectrum from Figure 7B, OH group and Si-H bond were detected only on the cantilever surface after laser exposure and etching. Si-H bondings are reported to show different peak position depends on the connectivity of Si atom; the peak at area I shows Si-H with Si atom connected to 3 oxygen (O_3SiH), and another slight peak around area II shows Si_3SiH .³⁰ On the other hands, the defects such as NBOHC ($\equiv\text{Si}-\text{O}\cdot$), ODC (II) ($\equiv\text{Si}\cdot$), and ODC (I) ($\equiv\text{Si}-\text{Si}\equiv$) structure were found at femtosecond laser irradiated spot.²⁹ Furthermore, silicon nanocluster could be generated with relatively low pulse energy with kilohertz repetition.³¹ Considering these facts, these defects might be the precursor and combined with H^+ during etching to generate OH groups and Si-H bondings. As a result, residual effect of laser exposure might remain after etching and formed distinctive surface compared to nonexposed. Higher roughness on exposed surface may also bring increment of OH groups, although extra modification was suggested by significant effect on reflection around 2000 cm^{-1} .

In addition to generation of functional groups, absorption peak around 1110 cm^{-1} shifted to higher wavenumber side at the cantilever surface. This peak can be correlated with the fused silica density. Generally, the upshift of this peak is due to an increase in the Si-O-Si bond angle. Moreover, this increment indicates a density decrease in silica glass.³² The shift was 2.5 cm^{-1} , and this is enough to induce 500 ppm reduction in silica density,³³ ending up in a decrease from 2201 to 2200 kg/m^3 . In the case of fused silica, a lower density has a correlation with lower etching rate.³⁴

In this experiment, FTIR measurements were observing the chemical bonding state down to 10 μm under the surface of the cantilever. These chemical properties change at the exposed surface indicates the generation of a silica layer with different material constants such as density and Young's modulus, consecutive to the micromachining process. As increment of OH contents in fused silica lowers the Young's modulus,³⁵ we considered the same effect is occurring on the cantilever surface containing terminal bondings like Si-OH and Si-H.

These material properties change affects the vibration characteristics, as shown in Equations 2–8. Experimental results for all cantilever showed a lower resonant frequency compared to the simulation, as shown in Figure 4. This difference can be explained by having a lower Young's modulus layer at the surface, as if an absorbing layer covers the cantilever. Model C in Figure 4 was plotted with empty diamonds, has lower material constants ($E_{\text{surface}} = 60 \text{ GPa}$) in a region of 10 μm below the exposed surface, supposing a residual effect of laser exposure and etching. Partial decrease in material

constants lowered the resonant frequency more than the dimensional error.

The surface of silica glass after femtosecond laser micromachining was modified, and this effect was analyzed qualitatively. At this point, the measurement of density and Young's modulus profile inside the glass sample was difficult. With further understanding of surface properties, quantitative analysis of damping effect based on ABH theory given in Krylov's report⁷ will be possible.

However, it seems clear that a key factor for ABH damping of microscale structure is not only the design of the shape but also the material properties change during the fabrication process. Lower Young's modulus provides a damping effect by lowering the reflection coefficient R as given in Equations 5 and 7. In the case of ABH effect implementation, this femtosecond laser-induced modification effectively enhanced the damping effect.

5 | CONCLUSION

In conclusion, an Acoustic Black Hole effect was observed in a fused silica microscale cantilever. It successfully showed the ABH effect with double-sided tapering taking advantage of microscale accurate machining using a femtosecond laser. In addition, the effect was realized in the lower-frequency range compared to previous reports. It is now possible to attenuate desirable frequency that depends on structural design with a wide variety of materials. Furthermore, additional damping layer of different material is unnecessary to enhance the ABH effect and to keep the optical transparency of the cantilever. In this way, the ABH effect can be applied in the field of micro-optical devices by combining factors such as microdimension and transparent material. This study is the first approach of ABH (vibration dynamics) toward micromechanical and optical systems.

It seemed all laser-affected area was washed away after etching, although residual exposure effects were observed through vibration test with various tapered length cantilevers. This modified layer affects the dynamic behavior of the microfabricated structural object, and gives an additional damping effect on micro-3D structural objects.

ORCID

Kana Tomita  <https://orcid.org/0000-0002-0575-0906>

Tetsuo Kishi  <https://orcid.org/0000-0002-8392-1360>

Yves Bellouard  <https://orcid.org/0000-0002-8409-4678>

REFERENCES

- Bellouard Y, Said A, Dugan M, Bado P. Fabrication of high-aspect ratio, micro-fluidic channels and tunnels using femtosecond laser pulses and chemical etching. *Opt Express*. 2004;12(10):2120–9.
- Tielen V, Bellouard Y. Three-dimensional glass monolithic micro-flexure fabricated by femtosecond laser exposure and chemical etching. *Micromachines*. 2014;5(3):697–710.
- Wang P, Chu W, Li W, Tan Y, Liu F, Wang M, et al. Three-dimensional laser printing of macro-scale glass objects at a micro-scale resolution. *Micromachines*. 2019;10(9):565.
- Marcinkevičius A, Juodkakis S, Watanabe M, Miwa M, Matsuo S, Misawa H, et al. Femtosecond laser-assisted three-dimensional microfabrication in silica. *Opt Lett*. 2001;26(5):277.
- Toshiyoshi H, Ju S, Honma H, Ji CH, Fujita H. MEMS vibrational energy harvesters. *Sci Technol Adv Mater*. 2019;20(1):124–43.
- Mironov MA. Propagation of a flexural wave in a plate whose thickness decreases smoothly to zero in a finite interval. *Sov Phys Acoust*. 1988;34(3):318–9.
- Krylov VV, Tilman FJBS. Acoustic “black holes” for flexural waves as effective vibration dampers. *J Sound Vib*. 2004;274(3–5):605–19.
- Krylov V. Conditions for validity of the geometrical-acoustics approximation in application to waves in an acute-angle solid wedge. *Sov Phys - Acoust*. 1989;35(2):176–80.
- Krylov VV, Winward RETB. Experimental investigation of the acoustic black hole effect for flexural waves in tapered plates. *J Sound Vib*. 2007;300(1–2):43–9.
- Krylov V. Acoustic black holes: Recent developments in the theory and applications. *IEEE Trans Ultrason Ferroelectr Freq Control*. 2014;61(8):1296–306.
- Hnatovsky C, Taylor RS, Simova E, Bhardwaj VR, Rayner DM, Corkum PB. Polarization-selective etching in femtosecond laser-assisted microfluidic channel fabrication in fused silica. *Opt Lett*. 2005;30(14):1867–9.
- Yang T, Bellouard Y. 3D electrostatic actuator fabricated by non-ablative femtosecond laser exposure and chemical etching. *International Symposium of Optomechatronics Technology (ISOT 2015)*. MATEC Web Conf. 2015;32:02003. 1–6. [Abstract paper – published].
- Qi J, Wang Z, Xu J, Lin Z, Li X, Chu W, et al. Femtosecond laser induced selective etching in fused silica: optimization of the inscription conditions with a high-repetition-rate laser source. *Opt Express*. 2018;26(23):29669–78.
- Hirao K, Miura K. Writing waveguides and gratings in silica and related materials by a femtosecond laser. *J. Non-Cryst*. 1998;239(1):91–5.
- Taylor RS, Hnatovsky C, Simova E, Rayner DM, Bhardwaj VR, Corkum PB. Ultra-high resolution index of refraction profiles of femtosecond laser modified silica structures. *Opt Express*. 2003;8(7):775–81.
- Vlugter P, Block E, Bellouard Y. Local tuning of fused silica thermal expansion coefficient using femtosecond laser. *Phys Rev Mater*. 2019;3(5):053802. 1–8.
- Bellouard Y, Colomb T, Depeursinge C, Dugan M, Said AA, Bado P. Nanoindentation and birefringence measurements on fused silica specimen exposed to low-energy femtosecond pulses. *Opt Express*. 2006;14(18):8360–6.
- Vlugter P, Bellouard Y. Elastic properties of self-organized nanogratings produced by femtosecond laser exposure of fused silica. *Phys Rev Mater*. 2020;4(2):023607. 1–7.
- Athanasidou CE, Bellouard Y. A monolithic micro-tensile tester for investigating silicon dioxide polymorph micromechanics, fabricated and operated using a femtosecond laser. *Micromachines*. 2015;6(9):1365–86.

20. Chan JW, Huser T, Risbud S, Krol DM. Structural changes in fused silica after exposure to focused femtosecond laser pulses. *Opt Lett*. 2001;26(21):1726–8.
21. Feurtado PA, Conlon SC, Semperlotti F. A normalized wave number variation parameter for acoustic black hole design. *J Acoust Soc Am*. 2014;136(2):EL148–EL152.
22. Rajesh S, Bellouard Y. Towards fast femtosecond laser micromachining of glass, effect of deposited energy. *Opt InfoBase Conf Pap*. 2010;18(20):21490–7.
23. Serhatlioglu M, Ortaç B, Elbuken C, Biyikli N, Solmaz ME. CO₂ laser polishing of microfluidic channels fabricated by femtosecond laser assisted carving. *J Micromech Microeng*. 2016;26(11):115011. 1–9.
24. Tomozawa M, Hong JW, Ryu SR. Infrared (IR) investigation of the structural changes of silica glasses with fictive temperature. *J Non Cryst Solids*. 2005;351(12–13):1054–60.
25. Davis KM, Tomozawa M. Water diffusion into silica glass: Structural changes in silica glass and their effect on water solubility and diffusivity. *J Non Cryst Solids*. 1995;185(3):203–20.
26. Sarikov A, Voitovych M, Lisovskyy I, Naseka V, Hartel A, Hiller D, et al. Characteristics of hydrogen effusion from the Si-H bonds in Si rich silicon oxynitride films for nanocrystalline silicon based photovoltaic applications. *Adv Mater Res*. 2014;854:69–74.
27. Bellouard Y, Champion A, McMillen B, Mukherjee S, Thomson RR, Pépin C, et al. Stress-state manipulation in fused silica via femtosecond laser irradiation. *Optica*. 2016;3(12):1285.
28. Streltsov AM, Borrelli NF. Study of femtosecond-laser-written waveguides in glasses. *J Opt Soc Am B*. 2002;19(10):2496–504.
29. Zoubir A, Rivero C, Grodsky R, Richardson K, Richardson M, Cardinal T, et al. Laser-induced defects in fused silica by femtosecond IR irradiation. *Phys Rev B - Condens Matter Mater Phys*. 2006;73(22):1–5.
30. Dřínek V, Vacek K, Yuzhakov G, Bastl Z, Naumov S. Hydrogen related point defects in silicon based layers: Si(•)H and SiOOH. *Surf Sci*. 2006;600(7):1462–7.
31. Reichman WJ, Krol DM, Shah L, Yoshino F, Araj A, Eaton SM, et al. A spectroscopic comparison of femtosecond-laser-modified fused silica using kilohertz and megahertz laser systems. *J Appl Phys*. 2006;99:123112. 1–5.
32. Devine RAB. Ion implantation- and radiation-induced structural modifications in amorphous SiO₂. *J Non Cryst Solids*. 1993;152(1):50–8.
33. Shelby JE. Density of vitreous silica. *J Non Cryst Solids*. 2004;349(1–3):331–6.
34. Agarwal A, Tomozawa M. Correlation of silica glass properties with the infrared spectra. *J Non Cryst Solids*. 1997;209(1–2):166–74.
35. Le Parc R, Levelut C, Pelous J, Martinez V, Champagnon B. Influence of fictive temperature and composition of silica glass on anomalous elastic behaviour. *J Phys Condens Matter*. 2006;18:7507–27.

How to cite this article: Tomita K, Kishi T, Yano T, Vlughter P, Bellouard Y. ABH damping of monolithic silica glass cantilever by structural and material modification using fs laser micromachining. *Int J Appl Glass Sci*. 2021;12:36–45. <https://doi.org/10.1111/ijag.15857>